Long-Range Order in Electronic Transport Through Disordered Metal Films

S. Aigner,[1,2] L. Della Pietra,[1] Y. Japha,[3] O. Entin-Wohlman,[3] T. David,[3] R. Salem,[3] R. Folman,[3] J. Schmiedmayer[1,2]*

Ultracold atom magnetic field microscopy enables the probing of current flow patterns in planar structures with unprecedented sensitivity. In polycrystalline metal (gold) films, we observed long-range correlations forming organized patterns oriented at ±45° relative to the mean current flow, even at room temperature and at length scales larger than the diffusion length or the grain size by several orders of magnitude. The preference to form patterns at these angles is a direct consequence of universal scattering properties at defects. The observed amplitude of the current direction fluctuations scales inversely to that expected from the relative thickness variations, the grain size, and the defect concentration, all determined independently by standard methods. Ultracold atom magnetometry thus enables new insight into the interplay between disorder and transport.

Thin metal films are the classic environment for studying the effect of geometric constraints (*1*, *2*) and crystal defects (*3*, *4*) on the transport of electrons. In a perfectly straight long wire that is free from structural defects, a direct current strictly follows the wire direction and creates a magnetic field in the plane perpendicular to the wire. An obstacle may locally change the direction of the current and consequently locally rotate the magnetic field close to the wire by an angle β in a plane parallel to the plane of the thin-film wire.

Ultracold atom magnetometry (*5*, *6*) on atom chips (*7*–*9*) allows for the sensitive probing of this angle β (and its spatial variation) with microrad (micrometer) resolution. Relative to scanning probes having micrometer-scale spatial resolution and 10^{-5} T sensitivity, or superconducting quantum interference devices (SQUIDs) having 10^{-13} T sensitivity but a resolution of tens of micrometers, ultracold atom magnetometry has both high sensitivity (10^{-10} T) and high resolution (several micrometers) (*6*). In addition, ultracold atoms enable high resolution over a large length scale (millimeters) in a single shot (*10*). This enables the simultaneous observation of microscopic and macroscopic phenomena, as described below.

Using cold atoms just above the transition to Bose-Einstein condensation (BEC), we applied ultracold atom magnetometry to study the current deflection in three different precision-fabricated polycrystalline gold wires with a rectangular cross section of 200 μm and different thicknesses and crystalline grain sizes (Table 1) (*11*). Choosing the wire length along x, its width along y, and its thickness along z, Fig. 1 shows the maps of the angular variations $\beta(x, y, z_0) = \delta B_x(x, y, z_0)/B_y$ of the magnetic field created by a current of 180 mA flowing along the wire, measured at $z_0 = 3.5$ μm above its center (far from the edges).

Even though scattering by lattice vibrations (phonons) quickly diffuses the electronic motion at ambient temperature, long-range correlations (tens of micrometers) in the current flow patterns can be seen. This is surprising, as the effects of static defects are usually observed only on a length scale of several nanometers (*12*, *13*). We observed clear patterns of elongated regions of maximal current flow deviations β inclined by about ±45° to the mean current flow direction. This angular preference was present in all the measurements, independent of wire thickness or grain size. This preference can be quantified by the normalized angular power spectra $p(\theta) = \int dk k|\beta(k, \theta)|^2$ of the magnetic field patterns, where $\mathbf{k}$ is the wave vector of the Fourier transform of the measured $\beta(x, y)$ (Fig. 1).

We observed considerable differences in the magnitude and spectral composition of the magnetic field variations above wires with different thicknesses. Table 1 summarizes the main observations and wire properties. The magnitude of β scales contrary to the surface corrugations when compared to the thickness; the thinner films (H = 280 nm) have the largest relative thickness variations but show the smallest current directional variations. Moreover, the thin wire with the large grains (grain size 150 to 170 nm) shows the smallest variations (β_{rms} = 39 μrad), much too small to be explained by the measured top surface roughness $\delta z_+^{rms}/H = 1.7 \times 10^{-3}$ of the gold film.

The observed magnetic field variations caused by the current direction variations are orders of magnitude smaller than those reported in studies of "fragmentation" of cold atom clouds on atom chips [for a review see (*9*)]. These previously reported fragmentation measurements can be fully explained by corrugations in the wire edges (*14*, *15*). In the present study, the effects caused by the wire edge roughness are strongly suppressed by the much-improved fabrication (*11*, *16*) and the flat, wide wire geometry (where the ratio between the distance to the wire surface and the distance to the wire edge is very high) (*17*).

To analyze the underlying mechanism for the current direction deviations, we consider a thin film (conductivity σ_0) in the x-y plane with a regular current $J_0\hat{x} = \sigma_0 \mathbf{E}^{(0)}$, where the electric field $\mathbf{E}^{(0)}$ is in the $\hat{x}$ direction. We consider the effect of small fluctuations in the conductivity $\delta\sigma(\mathbf{x})$ on the current flow (*10*). The current flow around a circular defect (Fig. 2, A and B) generates a dipole field with a transverse component $E_y^{(1)} \propto \sin 2\theta$ (*10*), causing the current field to be repelled from the defect (for $\delta\sigma < 0$) or attracted to the defect (for $\delta\sigma > 0$), and a 45° pattern in the transverse current flow forms.

A second illustration is a conductivity step ($\delta\sigma$) inclined by an angle θ to the current flow direction (Fig. 2C). The resulting current density fluctuation is

$$\delta\mathbf{J} = J_0 \frac{\delta\sigma}{\sigma_0} (\sin^2\theta\hat{x} - \cos\theta \sin\theta\hat{y}) \qquad (1)$$

Table 1. Properties of the wires under investigation [see text and (*10*) for definitions]. All measurements were done on the chip used for the cold atom experiment except for the low-temperature resistivity, which was measured on a duplicate chip made with an identical (simultaneous) fabrication process (*10*).

Wire	A	B	C
Thickness H (μm)	2.08	0.28	0.28
Grain size (nm)	60 to 80	30 to 50	150 to 170
Resistivity at 296 K (μohm·cm)	2.73	3.1	2.77
Resistivity at 4.2 K (μohm·cm)	0.094	0.316	0.351
Atom temperature (nK)	286 ± 15	173 ± 2	92 ± 7
Measurement height (μm)	3.5 ± 0.4	3.4 ± 0.3	3.7 ± 0.4
δz_+^{rms} (atomic force microscope) (nm)	9.4	3.5	3.1
δz_+^{rms} (white-light interferometer) (nm)	1.31	0.42	0.48
$\delta z_+^{rms}/H$ (white-light interferometer) ($\times 10^{-3}$)	0.629	1.500	1.714
β_{rms} (mrad)	0.168	0.0715	0.0388
β_{pp} (mrad)	0.4	0.2	0.1
λ_β (μm)	77	46	48

[1]Physikalisches Institut, Universität Heidelberg, Philosophenweg 12, 69120 Heidelberg, Germany. [2]Atominstitut der Österreichischen Universitäten, Technische Universität Wien, Stadionalle 2, 1020 Vienna, Austria. [3]Department of Physics, Ben-Gurion University of the Negev, P.O. Box 653, Be'er-Sheva 84105, Israel.

*To whom correspondence should be addressed. E-mail: schmiedmayer@atomchip.org

(*10*). The transverse current component J_y is again proportional to sin 2θ, which is maximal for conductivity steps inclined by θ = ±45°.

In a metal film, we expect to find a random pattern of conductivity fluctuations δσ(**x**). It can be constructed from a random spatial distribution of the above basic elements: microscopic circular defects or macroscopic conductivity steps of different angles. The relation between the microscopic and macroscopic phenomena for each of these models is described in (*10*).

For a general quantitative analysis, we expand an arbitrary distribution δσ(**x**) in a Fourier series of plane waves of the form $\delta\sigma(\mathbf{x}) = \delta\sigma_{\mathbf{k}} \sin(\mathbf{k}\cdot\mathbf{x} + \phi)$, where $\mathbf{k} = (k_x, k_y) = k(\cos\theta_{\mathbf{k}}, \sin\theta_{\mathbf{k}})$ and φ is an arbitrary phase. Each plane wave contributes to the current fluctuation angle $\alpha = \delta J_y/J_0$ according to Eq. 1, giving $\alpha(\mathbf{k}) \approx -\sin 2\theta_{\mathbf{k}}\,(\delta\sigma_{\mathbf{k}}/2\sigma_0)$ and resulting in the observed 45° pattern.

The resulting magnetic field angle fluctuations at height z above the wire is directly related to the current fluctuations by

$$\beta(\mathbf{k}, z) \approx \exp(-kz)\alpha(\mathbf{k}) \approx -\frac{1}{2}\exp(-kz)\frac{\delta\sigma_{\mathbf{k}}}{\sigma_0}\sin 2\theta_{\mathbf{k}} \qquad (2)$$

which exhibits the same angular dependence. The exponential term exp(–kz) represents a resolution limit, such that the effects of current changes on a length scale smaller than 2πz are suppressed in the spectrum of the magnetic field fluctuations. Starting from random conductivity fluctuations with a nonwhite spatial frequency distribution, the angular dependence sin 2θ will emerge, giving rise to the observed ±45° preference. We have simulated such random models, and the observable β forms two-dimensional (2D) maps similar to those in Fig. 1 (*10*). The variations δσ(**x**) in the conductivity σ in a thin metal film are caused by contributions from two physical origins: (i) bulk conductivity variations in the metal, and (ii) variations in the boundaries, namely variations in the thickness H of the film δH(**x**) leading to a change in the conductivity per unit area $\delta\sigma = \sigma_0\delta H/H$.

To investigate whether the observed current flow deviations are related to corrugations in the top surface of the wire, we measured the surface topography of the wires with a white-light interferometer. No angular preference inherent in the structure of the wires was found. Consequently, the angular pattern in the magnetic field variations presented in Fig. 1 must be a pure property of the scattering mechanism of the current flow by the wire defects, as outlined above. Moreover, when we calculated the 2D magnetic field at 3.5 μm above the surface, using the white-light interferometry measurements and the assumption δH(**x**) = δz_+(**x**), we could not find a reasonable fit between the latter and the magnetic mapping done by the atoms (Fig. 1). A detailed analysis of the top surface corrugations δz_+ (Fig. 3) shows that they are significantly larger for the thick film than for the two thin films, especially at short length scales.

To quantify our findings, we compared the power spectra of the measured magnetic field variations to those calculated from several models on the basis of the measured top surface variations, an assumed bottom surface roughness, and possible inhomogeneities in the bulk conductivity (Fig. 4). For the two thin wires B and C, the measured power spectra of the magnetic field variations are lower (by two orders of magnitude for large wavelengths) than predictions based on a model with a flat bottom surface (δH = δz_+). If we assume that the top surface exactly follows the bottom surface (δz_+ = δz_-), a lower bound on the influence of the surface on magnetic field fluctuations can be obtained, as this configuration produces vertical currents whose contribution to the longitudinal magnetic field, to which our experiment is sensitive, is very small. The measured data are in between these two cases.

A fair fit of the measured spectrum for the thin wires is obtained if we assume that the top surface partially follows the large-wavelength fluctuations of the bottom surface, whereas independent fluctuations of the top surface exist in the shorter scale. For such a model (*10*), we assume $\delta z_-(k) \approx \delta z_+(k)\,\exp[-(k/k_0)^2]$. Note that the resulting average thickness variations are

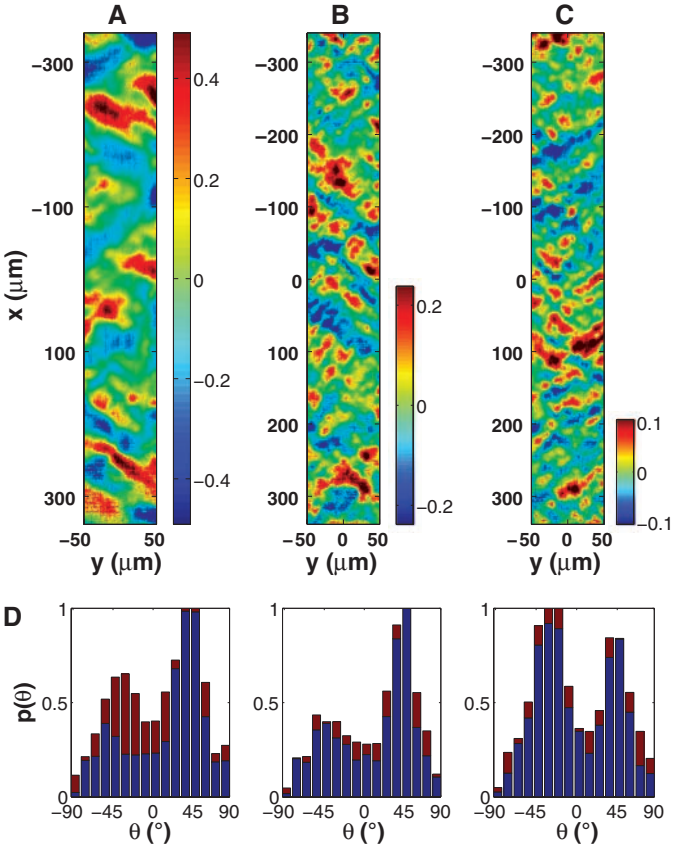

Fig. 1. (**A** to **C**) Magnetic field angle fluctuations β (color scale bars, mrad) above the three different polycrystalline gold films described in Table 1. These fluctuations are due to variations in the direction of the current flow and are thus sensitive to δJ_y. The appearance of ±45° patterns is clearly observable and reflects a correlated scattering of the electrons. (**D**) Quantification of the angular pattern by the normalized angular power spectral density $p(\theta)/\max(p)$. The red bars indicate the uncertainties given by different procedures to account for the finite size of the sample.

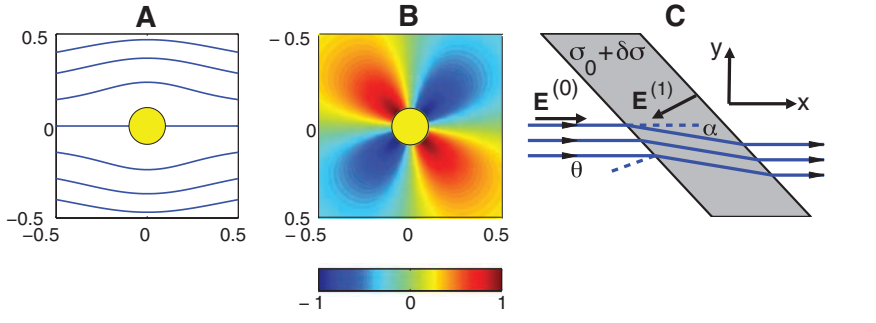

Fig. 2. (**A**) Current scattering by circularly symmetric (disk) local conductivity variations δσ < 0. (**B**) The transverse ($\hat{y}$) component of the current is proportional to sin 2θ. (**C**) Direction change of a current flow due to a conductivity step defect inclined by an angle θ relative to the current flow direction $\hat{x}$. The conductivity is σ_0 everywhere except in the shaded area, where it is $\sigma_0 + \delta\sigma$ (δσ > 0 in this example). Again, the electron scattering amplitude is proportional to sin 2θ. For details see (*10*).

extremely small: $\delta H^{rms} < 1$ Å (with $\delta H = \delta z_+^{rms} - \delta z_-^{rms}$). This value of δH^{rms} refers to length scales longer than 1 μm, whereas atomic force microscope measurements showed much larger surface variations on the scale of the grains (Table 1).

The situation is different for the thick wire A ($H = 2$ μm). Models assuming a flat bottom surface ($\delta H = \delta z_+$) underestimate the measured magnetic field variations, as do models assuming a corrugated bottom surface δz_- with a spectrum similar to that of wire B and no correlations with the top surface. The difference between the surface models and the measured data of wire A can be attributed to fluctuations in the bulk conductivity. A model taking the maximal contribution of surface roughness (uncorrelated top and bottom surfaces) into account gives the minimal required contribution of the bulk conductivity fluctuations (*10*). If we apply the same minimal bulk conductivity fluctuations as obtained from wire A to the two thin wires B and C, they overestimate the measured magnetic field fluctuations substantially for both wires and give a different spectral shape. This indicates that the bulk conductivity of the thinner wires should be more homogeneous than that of the thick wire.

A more homogeneous bulk conductivity in the thin wires, however, appears to be contradictory to the fact that the low-temperature resistivity is smaller for the thick wire than for the thin wires (Table 1). Nonetheless, we note that this resistivity is mainly determined by the small-scale properties of the wire (on the order of the grain size or less) and by surface scattering, whereas the magnetic field variations probe the conductivity inhomogeneities at a larger scale and provide complementary information that would not be available by standard methods.

Our analysis furthermore suggests (*10*) that the differences in the length scale λ_β of the variation in β, as seen in Fig. 1 and quantified in Table 1, may originate from the fact that conductivity variations in the thin wires (a result of thickness variations) are suppressed at long length scales because of top and bottom surface correlations. In contrast, conductivity variations in the thick wire originate at all scales from a combination of thickness variations due to uncorrelated top and bottom surfaces and a dominant contribution of bulk conductivity inhomogeneity.

Our study constitutes a direct application of ultracold atoms as a probe for solid-state science. The exceptional sensitivity of the ultracold atom magnetic field microscope (*5*, *6*) allowed us to observe long-range patterns of the current flow in a disordered metal film. The preference of features with angles around ±45° in the measured angular spectrum of the current flow fluctuations is due to the universal scattering properties at defects. A detailed quantitative analysis reveals that the observed current directional fluctuations at different wires exhibit diverse and unexpected properties due to different physical origins. Our results clearly demonstrate the power of the ultracold atom magnetic field microscope to study details of the current flow in conductors, as well as its ability to reveal previously inaccessible information. This technique may be expected to stimulate new studies of the interplay between disorder and coherent transport in a variety of systems ranging from high-T_c superconductors (*18*) to 2D electron gases (*19*) and nanowires (*20*).

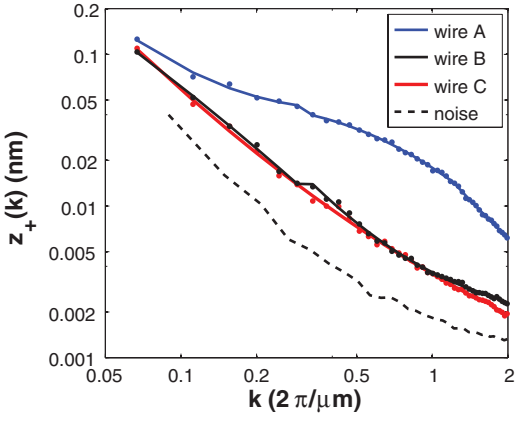

Fig. 3. Radial spectrum of the top surface corrugations $|\delta z_+(k)| = [(2\pi)^{-1}\int d\theta |\delta z_+(k, \theta)|^2]^{1/2}$ for the three wires measured with a white-light interferometer. Note the considerable difference between wire A and wires B and C. Measurement noise level was calculated by averaging over many partly overlapping images (*10*).

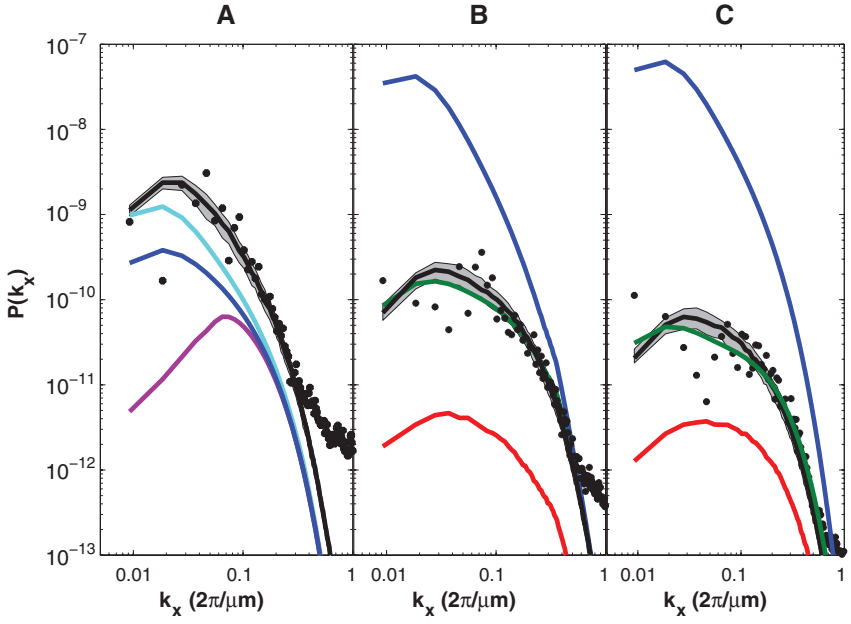

Fig. 4. Comparison of surface and bulk model calculations (lines) with the measured power spectrum $P(k_x) = \sum_{k_y} |\beta(k_x, k_y)|^2$ of the magnetic field angle β along the *x* direction above the three wires (points). Blue: Top surface δz_+ as in Fig. 3 with flat bottom surface $\delta z_- = 0$. Red: Top surface follows bottom surface $\delta z_+ = \delta z_-$ (i.e., no thickness variations). Green: Partially correlated top and bottom surfaces for wires B and C. For the thick wire A, we assume $\delta z_-(k)$ as in wire B, which is correlated (purple) or uncorrelated (light blue) with the top surface. The latter gives the closest estimate for the experimental data but gives a β_{rms} value that is only about half of the measured value. Black: A fit to a model assuming bulk conductivity fluctuations. The shaded area represents a 1-SD range obtained by varying the relative phases of different spectral components $\delta\sigma(k_x, k_y)$. See (*10*).

References and Notes

1. E. H. Sondheimer, *Adv. Phys.* **1**, 1 (1952).
2. R. G. Chambers, *Proc. R. Soc. London Ser. A* **202**, 378 (1950).
3. A. F. Mayadas, M. Shatzkes, *Phys. Rev. B* **1**, 1382 (1970).
4. R. Landauer, *IBM J. Res. Dev.* **1**, 223 (1957).
5. S. Wildermuth *et al.*, *Nature* **435**, 440 (2005).
6. S. Wildermuth *et al.*, *Appl. Phys. Lett.* **88**, 264103 (2006).
7. R. Folman, P. Krüger, J. Schmiedmayer, J. Denschlag, C. Henkel, *Adv. At. Mol. Opt. Phys.* **48**, 263 (2002).
8. J. Reichel, *Appl. Phys. B* **74**, 469 (2002).
9. J. Fortagh, J. C. Zimmermann, *Rev. Mod. Phys.* **79**, 235 (2007).
10. See supporting material on *Science* Online.
11. The chip was fabricated at the Weiss Family Laboratory for Nanoscale Systems, Ben-Gurion University, Israel (www.bgu.ac.il/nanofabrication).
12. W. Steinhögl, G. Schindler, G. Steinlesberger, M. Engelhardt, *Phys. Rev. B* **66**, 075414 (2002).
13. M. A. Schneider, M. Wenderoth, A. J. Heinrich, M. A. Rosentreter, R. G. Ulbrich, *Appl. Phys. Lett.* **69**, 1327 (1996).
14. D.-W. Wang, M. D. Lukin, E. Demler, *Phys. Rev. Lett.* **92**, 076802 (2004).
15. T. Schumm *et al.*, *Eur. Phys. J. D* **32**, 171 (2005).
16. S. Groth *et al.*, *Appl. Phys. Lett.* **85**, 2980 (2004).
17. P. Krüger *et al.*, *Phys. Rev. A* **76**, 063621 (2007).

18. D. A. Bonn, *Nat. Phys.* **2**, 159 (2006).
19. S. Ilani, A. Yacoby, D. Mahalu, H. Shtrikman, *Science* **292**, 1354 (2001).
20. J. Feist *et al.*, *Phys. Rev. Lett.* **97**, 116804 (2006).
21. We thank the team of the Ben-Gurion University Weiss Family Laboratory for Nanoscale Systems for the fabrication of the chip, and J. Jopp of the Ben-Gurion University Ilse Katz Center for Nanoscale Science for assisting with surface measurements. R.F. thanks Y. Imry and A. Klug for their continued support. Supported by the Fonds zur Förderung der Wissenschaftlichen Forschung, Deutsche Forschungsgemeinschaft, German Federal Ministry of Education and Research (Deutsch-Israelische Projektkooperation), European Community "Atomchip" Research Training Network, American-Israeli Binational Science Foundation, and Israeli Science Foundation.

Supporting Online Material
www.sciencemag.org/cgi/content/full/319/5867/1226/DC1
Materials and Methods
Figs. S1 to S3
References

1 November 2007; accepted 7 January 2008
10.1126/science.1152458

Chemically Derived, Ultrasmooth Graphene Nanoribbon Semiconductors

Xiaolin Li,* Xinran Wang,* Li Zhang, Sangwon Lee, Hongjie Dai†

We developed a chemical route to produce graphene nanoribbons (GNR) with width below 10 nanometers, as well as single ribbons with varying widths along their lengths or containing lattice-defined graphene junctions for potential molecular electronics. The GNRs were solution-phase–derived, stably suspended in solvents with noncovalent polymer functionalization, and exhibited ultrasmooth edges with possibly well-defined zigzag or armchair-edge structures. Electrical transport experiments showed that, unlike single-walled carbon nanotubes, all of the sub–10-nanometer GNRs produced were semiconductors and afforded graphene field effect transistors with on-off ratios of about 10^7 at room temperature.

Graphene (single-layer graphite) has emerged as a material with interesting low-dimensional physics and potential applications in electronics (*1*–*6*). Graphene nanoribbons (GNRs), if made into quasi-one-dimensional structures with narrow widths (<~10 nm) and atomically smooth edges, are predicted to exhibit band gaps useful for room-temperature transistor operations with excellent switching speed and high carrier mobility (potentially even ballistic transport) (*7*–*13*). Recent theoretical work predicted that quantum confinement and edge effects make narrow GNRs (width w < ~10 nm) into semiconductors, which differs from single-walled carbon nanotubes (SWNTs) that contain ~1/3 metallic species.

Lithographic patterning of graphene sheets has fabricated GNRs down to widths of ~20 nm thus far (*12*, *13*), but there are difficulties in obtaining smooth edges (for example, with roughness < ~5 nm) and reaching true nanometer-scale ribbon width. Chemical approaches (*14*–*17*) and self-assembly processes may produce graphene structures with desired shape and dimensions for fundamental and practical applications.

We report that, by using a widely available and abundant graphite material, we can develop simple chemical methods to produce GNRs. We exfoliated commercial expandable graphite (Grafguard 160-50N, Graftech Incorporated, Cleveland, OH) by brief (60 s) heating to 1000°C in forming gas (3% hydrogen in argon). The resulting exfoliated graphite was dispersed in a 1,2-dichloroethane (DCE) solution of poly(m-phenylenevinylene-co-2,5-dioctoxy-p-phenylenevinylene) (PmPV) by sonication for 30 min to form a homogeneous suspension. Centrifugation then removed large pieces of materials from the supernatant (Fig. 1A and fig. S1) (*18*).

We used atomic force microscopy (AFM) to characterize the materials deposited on substrates from the supernatant and observed numerous GNRs with various widths ranging from w ~ 50 nm down to sub-10 nm (Fig. 1, B to F). Topographic heights of the GNRs (average length ~ 1 μm) were mostly between 1 and 1.8 nm, which correspond to a single layer (e.g., Fig. 1B, left image) or a few layers (mostly ≤3 layers). Smooth edges were observed for the GNRs, with edge roughness well below ribbon width even for $w \leq 10$ nm. Accurate measurements of GNR width were difficult because of the finite AFM tip radius (~10 to 20 nm), especially for ultranarrow ribbons. To circumvent the problem, we used the same tips to measure the apparent widths of Hipco (Carbon Nanotechnologies Incorporated, Houston, TX)

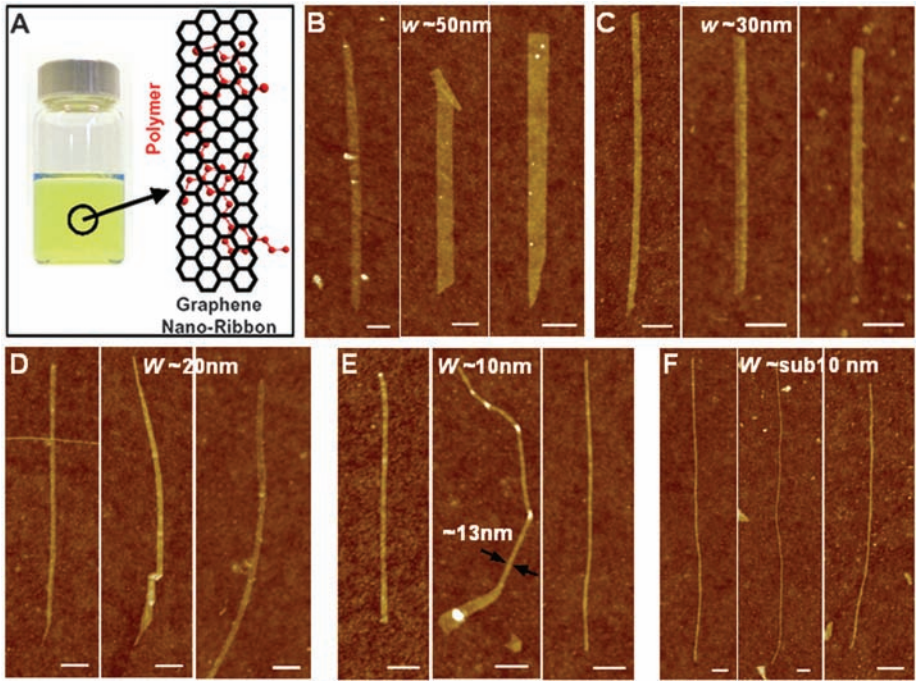

Fig. 1. Chemically derived graphene nanoribbons down to sub-10-nm width. (**A**) (Left) Photograph of a polymer PmPV/DCE solution with GNRs stably suspended in the solution. (Right) Schematic drawing of a graphene nanoribbon with two units of a PmPV polymer chain adsorbed on top of the graphene via π stacking. (**B** to **F**) AFM images of selected GNRs with widths in the 50-nm, 30-nm, 20-nm, 10 nm and sub-10-nm regions, respectively. A substrate (300-nm-thick $SiO_2/p^{++}Si$) was soaked in a GNR suspension for 20 min for deposition, rinsed, blow-dried, and calcined at 400°C to remove PmPV before AFM. Some of the GNRs narrow down to a sharp point near the ends. In (B), left ribbon height ~ 1.0 nm, one layer; middle ribbon height ~ 1.5 nm, two layers; right ribbon height ~ 1.5 nm, two layers. In (C), the three GNRs are two to three layers thick. In (D), ribbons are one (right image) to three layers. Two GNRs crossing in the left image are observed. In (E), ribbons are two- to three-layered. In the middle image, a single ribbon exhibits varying width along its length with mechanical bends (bright regions) between segments. In (F), the heights of the ultranarrow ribbons are ~1.5, 1.4, and 1.5 nm, respectively. All scale bars indicate 100 nm.

Department of Chemistry and Laboratory for Advanced Materials, Stanford University, Stanford, CA 94305, USA.

*These authors contributed equally to this work.
†To whom correspondence should be addressed. E-mail: hdai@stanford.edu